Available online at www.sciencedirect.com
ScienceDirect
Fusion Engineering and Design 82 (2007) 189–206
Fusion Engineering and Design
www.elsevier.com/locate/fusengdes

Identification of material parameters of a thermo-mechanical model for pebble beds in fusion blankets

Yixiang Gan, Marc Kamlah *

Forschungszentrum Karlsruhe, Postfach 3640, D-76021 Karlsruhe, Germany

Received 19 May 2006; received in revised form 15 September 2006; accepted 19 September 2006
Available online 23 October 2006

Abstract

In this paper, a thermo-mechanical model of pebble beds is adopted [D. Hofer, M. Kamlah, Drucker-Prager-Cap creep modelling of pebble beds in fusion blankets, Fusion Eng. Des. 73 (2005) 105–117] and developed based on experiments by Dr. Reimann at Forschungszentrum Karlsruhe (FZK). The framework of the present material model is composed of a non-linear elastic law [O. Coube, Modelling and numerical simulation of powder die compaction with consideration of cracking, PhD Thesis, University Pierre et Marie, Paris VI, 1998], the Drucker-Prager-Cap theory [ABAQUS, Analysis User's Manual, Version 6.5, 2004], a modified creep law [D. Hofer, M. Kamlah, Drucker-Prager-Cap creep modelling of pebble beds in fusion blankets, Fusion Eng. Des. 73 (2005) 105–117]. Furthermore, the volumetric inelastic strain dependent thermal conductivity of beryllium pebble beds [J. Reimann, G. Piazza, Z. Xu, A. Goraieb, H. Harsch, Measurements of the thermal conductivity of compressed beryllium pebble beds, FZKA 7096 (2005)] is taken into account and full thermo-mechanical coupling is considered.

By analyzing the deformation mechanism of the oedometric experiments, a new method is developed to determine the set of material parameters, including the temperature dependent hardening law. With the new method, the material parameters can be derived directly from the empirical equations (the so-called "Reimann fits" for pebble beds) including the thermoplastic behaviour. All these thermo-mechanical constitutive laws are implemented in ABAQUS by user defined field (USDFLD) and CREEP subroutines. The oedometric compression tests and creep tests under different temperatures are simulated by the present model, and the results show that the model gives a good description of experimental results. The analysis on the precompaction procedure of pebble beds assembly (PBA) is applied to show the feasibility of the present material model.

Keywords: Pebble beds; Constitutive modelling; Drucker-Prager-Cap theory; Creep; Thermal conductivity

1. Introduction

In the development of fusion technology, pebble beds are used in the helium-cooled pebble bed (HCPB) blanket. There are three main functions of the HCPB blanket: besides transformation of the neutron energy

* Corresponding author. Tel.: +49 7247 82 5860; fax: +49 7247 82 2347.
E-mail address: marc.kamlah@imf.fzk.de (M. Kamlah).

0920-3796/$ – see front matter © 2006 Elsevier B.V. All rights reserved.
doi:10.1016/j.fusengdes.2006.09.005

originating from the fusion reaction into usable heat and shielding of the superconducting magnets against neutron and gamma radiation, its main purpose is breeding of the fuel tritium by capturing neutrons in lithium [5,6]. Two main types of pebble beds are used in HCPB blanket: first ceramic pebble beds as breeder material, such as lithium orthosilicate (Li_4SiO_4); second beryllium pebble beds as neutron multiplier. The blanket is split into several modules filled with breeder and neutron multiplier pebble beds. The pebble beds are composed of nearly spherical shaped pebbles, whose diameters range from 0.25 to 2 mm [7]. Due to the extreme working conditions in the fusion reactor, a deep understanding of the thermo-mechanical properties of these pebble beds is essential. Thus, a material model for describing their response to the external excitation is needed, to check the requirements in design and analysis of the HCPB blanket.

For the thermo-mechanical modelling of pebble beds, there are several recent approaches in development. As a type of the discrete material, similar to sand, pebbles can be modeled by both a discrete element method (DEM) and a continuum approach.

In the first type of modelling, by means of the so-called discrete element method, the contact interactions and deformations of particles are analyzed in view of the constitutive modelling of pebble beds. As one issue, thermal creep of a ceramic breeder pebble bed is investigated by 3D discrete numerical thermomechanics code [8,9]. Other researchers [10–12] simplify the particles in regular lattices as beam elements, which represent the contact effects between pebbles. Considering the microstructures of pebble beds, the deformation mechanism can be clearly revealed by DEM approach, including the mechanical behaviours, thermal creep and the thermal conductivity. The physical meanings of some phenomenological material parameters can be better understood by this approach, such as the strain dependent thermal conductivity. But the problem remains, for example, that the complexity of the microstructure and the plastic contact of pebbles are still idealized in this approach. Furthermore, the plastic deformation of pebble beds results from a combination of the plastic deformations and the irreversible movements/rearrangements of pebbles, while in DEM, it is difficult to deal with the later effect.

The second type of modelling, considering materials composed of particles as continuous media, is the thermo-mechanical modelling in the framework of continuum mechanics. To take into account the typical material behaviour in engineering analyses, a corresponding phenomenological constitutive model can be exploited in the framework of the finite element method. By investigation of granular materials, many different models are developed in soil mechanics, such as the Drucker-Prager-Cap model and the Cam-Clay model. It should be noted that whether it is appropriate to use a continuum approach depends on the ratio of the size of the microstructure, i.e. an individual particle, compared to the dimension of the component under investigation. In the activities of FZK [1,13], the modified Drucker-Prager-Cap theory, which is one of the most frequently used models in soil mechanics, is applied as the constitutive model for pebble beds. The predictions of the model generally agree with the experiments, if the material parameters are chosen properly. However, in some specific cases unrealistic plastic softening behaviour of the Drucker-Prager-Cap model during unloading is observed. In the activities of Dipartimento di Ingegneria Nucleare (DIN, Palermo), Di Maio et al. [14] use both the Drucker-Prager-Cap model and the Gurson's model as plasticity laws, combined with a so-called the hyperporous elasticity law to analyze the SCATOLA benchmark experiments. Motivated by experimental results and by the empirical loading and unloading curves proposed by Reimann, Fokkens [15] applies two different elasticity laws for loading and unloading. This model is implemented in the finite element code MARC and used to analyze the thermo-mechanical behaviour of the pebble bed assembly (PBA) in pre-compaction and start-up procedures.

The aim of both approaches mentioned above is to represent the constitutive behaviours of the materials under the framework of different models. And the agreement between the prediction of model and the experimental results, such as oedometric compression, is the key to show the applicability of material models. In this investigation, the continuum approach is used for the modelling of the thermo-mechanical behaviours of pebble beds. Since the ratio of pebble size to the bed dimension is sufficiently small, this appears to be justified for both the experimental and the theoretical investigations.

The present material model is mainly based on systematical thermo-mechanical experiments [4,7,16–19] and a modified Drucker-Prager-Cap theory [1]. By

analyzing the macroscopic deformation mechanism of the oedometric test, a new method was developed to identify the possible set of material parameters in the Drucker-Prager-Cap theory, including the temperature dependent hardening law. With the new method, the empirical equations representing the experimental data for pebble beds, the so-called Reimann fits, can be used directly. In particular, the thermo-plastic behaviour of pebble beds is represented in terms of the temperature-dependence in the hardening law. Furthermore, the strain dependence of the thermal conductivity of beryllium pebble beds is taken into consideration in the present model.

This model is implemented in ABAQUS by user subroutines (USDFLD and CREEP, see ref. [3]). Several comparisons between the predictions of model and experiments are shown in this paper.

This paper is organized as follows. In Section 2, the present constitutive model for the representation of the material properties mentioned above is introduced. The analysis of the oedometric experiments and the method of the determination of material parameters from experimental data and empirical curves are discussed in Section 3, with special emphasis on the hardening law in the Drucker-Prager-Cap theory. The validations of the present thermo-mechanical model are listed in Section 4, and the improvement brought about by the present identification method and the validation of the resulting model is discussed. Furthermore, in Section 4, the present model is applied in the analysis of the pre-compaction procedure of pebble beds assembly. A few conclusions on the model and the obtained results are drawn in Section 5.

2. Constitutive modelling of pebble beds

In the HCPB concept, a pebble bed has typical dimensions on the order of 10^{-1} m, but is composed of nearly spherical particles with a typical diameter of 10^{-3} m. Thus, a continuum mechanics approach is appropriate for the investigation of the thermo-mechanical response to external excitation.

The main experimental phenomena of pebble beds are non-linear elasticity, volumetric plasticity, volumetric creep and strain dependent thermal conductivity. To describe the thermo-mechanical behaviour of pebble beds, the present material model is mainly based on the following: a non-linear elasticity law describes the observed stress dependent elasticity; the modified Drucker-Prager-Cap model predicts the yielding and hardening behaviour; the time-dependent behaviour or the thermal creep is modelled by a so-called consolidation (cap) creep mechanism; finally, the strain dependent thermal conductivity and the thermal expansion obtained in experiments are also implemented in the present material model. In this section, the present material model will be discussed in detail.

2.1. Non-linear elasticity law

For stress states inside the yield surface, it is assumed that the material behaves elastically. During unloading and reloading in the experiments (oedometric compression experiments), non-linear and non-hysteretic behaviour is observed. Since in the experiment, the unloading paths are parallel at different deformation levels, we consider the non-linear elastic properties a function of the stresses. The work of Coube [2] on powder die compaction deals with a material with microstructure having similar character as the pebble beds under consideration in this work. Therefore, the non-linear elasticity law proposed by Coube is adopted for the present material model. This law possesses the structure of the classical Hooke's law, however, Young's modulus dependents on the current stress state via the von Mises stress q and the hydrostatic pressure p in the form:

$$E = A_{\mathrm{e}}\left[\frac{1+\nu}{3}q^2 + 3\left(\frac{1}{2}-\nu\right)p^2\right]^{s/2} + E_0. \qquad (1)$$

Here, A_{e}, s and E_0 are material parameters, ν the Poisson's ratio and q and p may be expressed in terms of the principle stresses as:

$$q = \sqrt{\frac{1}{2}[(\sigma_1-\sigma_2)^2 + (\sigma_2-\sigma_3)^2 + (\sigma_1-\sigma_3)^2]}$$
$$p = -\frac{\sigma_1+\sigma_2+\sigma_3}{3} \qquad (2)$$

Fig. 1 gives an example of the contours of Young's modulus according to Eq. (1) in the q–p plane, and the shape of the contours are controlled by material parameters ν and s. This non-linear elasticity law has been

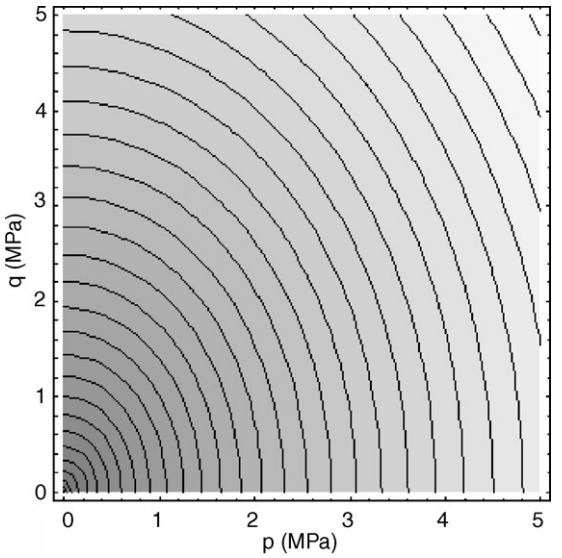

Fig. 1. The contour plot of Young's modulus (Eq. (1)) in the q–p plane ($\nu = 0.25$, $s = 0.6$).

implemented by a user-defined-field routine (USDFLD) in ABAQUS [1].

2.2. Drucker-Prager-Cap theory

In the present model, the plasticity of pebble beds is described by the Drucker-Prager-Cap model, which is a commonly used in geomechanics. This model has been implemented in the commercial finite element program ABAQUS [3] representing the yielding, hardening and time-dependent mechanical behaviour. The yield surface consists of the shear failure surface F_s and the cap surface F_c. Fig. 2 gives a representation of

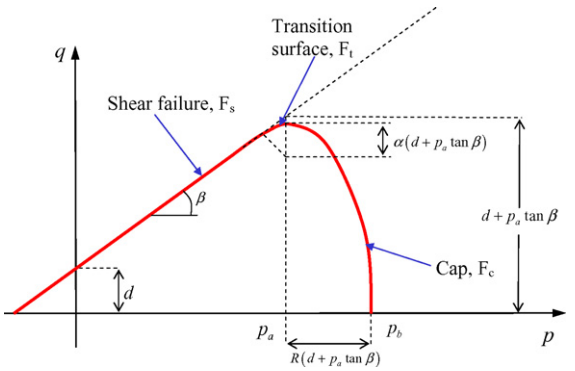

Fig. 2. The Drucker-Prager-Cap model (ABAQUS [3]).

the Drucker-Prager-Cap model in q–p plane. The shear failure surface F_s characterizes the pressure-dependent shear failure loading: as the pressure increases, a higher shear loading is needed to initiate shear failure. The cap surface F_c describes the plastic behaviour under the hydrostatic compression, which is not present in classical metal plasticity.

2.2.1. Formulas and material parameters

In detail, the yield criterion F_s and the non-associated plastic flow-potential G_s for shear failure surface are defined as:

$$\begin{aligned} F_s &= q - p\tan\beta - d = 0 \\ G_s &= \sqrt{[(p - p_a)\tan\beta]^2 + (q)^2}, \end{aligned} \tag{3}$$

where

$$p_a = \frac{p_b - Rd}{1 + R\tan\beta}. \tag{4}$$

For the cap surface, the yield criterion F_c and the associated flow-potential G_c read as:

$$\begin{aligned} F_c &= \sqrt{(p - p_a)^2 + (Rq)^2} - R(d + p_a\tan\beta) = 0 \\ G_c &= \sqrt{(p - p_a)^2 + (Rq)^2} \end{aligned}. \tag{5}$$

The plastic flow-potentials G_c and G_s are parts of ellipses forming together a continuous and smooth potential surface. There are several material parameters that need to be identified, such as the constants β, R, d and the material function p_b.

Constant β is the Drucker-Prager friction angle defining the slope of the shear failure surface F_s. It is not identical with the friction angle of granular materials, and the relation between these two "friction angles" will be discussed in Section 4.2. Constant d represents the value of the von Mises stress related to the cohesion of the material. For the pebble beds under consideration here, the value of d is almost to 0. Constant R controls the shape of the elliptic cap surface F_c. Finally, p_b defines the position of ellipse F_c. The dependence of p_b on the loading history is assumed to represent the hardening properties of material under consideration. For instance, in ABAQUS p_b is taken to be function of the inelastic volumetric strain, i.e. $p_b(\varepsilon_{vol}^{in})$ (default with "*CAP HARDENING"). Furthermore, it is also

possible to implement a plastic volumetric hardening law $p_b(\varepsilon_{vol}^{pl})$ or a work hardening law by a USDFLD routine.

2.2.2. Plastic flow theory

Since the plastic flow rule of Drucker-Prager-Cap model is not given in detail in the ABAQUS manual, they will be deduced in the following. We discuss the plastic flow in multi-surface and non-associated plasticity with $f^I(\sigma,\kappa)=0$ and $G^I(\sigma)$ as the I-th yielding (failure) criterion and the plastic flow-potential, correspondingly, where κ is a hardening parameter (an internal variable). For instance, in the Drucker-Prager-Cap model, Eqs. (3) and (5) give the description of yield (failure) surfaces and the plastic flow-potentials on the shear failure surface and cap surface, respectively. The plastic strain increments can be written as

$$d\varepsilon_{ij}^{pl} = \sum_{I=1}^{I_0} d\lambda \frac{\partial G^I}{\partial \sigma_{ij}}, \tag{6}$$

where $d\lambda$ is a factor of proportionality and I_0 is the number of the active yield surfaces. If the I-th yield (failure) surface is active, the corresponding consistency condition gives by differentiation

$$df^I = \frac{\partial f^I}{\partial \sigma_{ij}} d\sigma_{ij} + \frac{\partial f^I}{\partial \kappa} d\kappa = 0, \tag{7}$$

or in another form

$$\alpha^T d\sigma - A\, d\lambda = 0, \tag{8}$$

where

$$\alpha = \frac{\partial f^I}{\partial \sigma} = \left[\frac{\partial f^I}{\partial \sigma_{11}}, \frac{\partial f^I}{\partial \sigma_{22}}, \frac{\partial f^I}{\partial \sigma_{33}}, \frac{\partial f^I}{\partial \sigma_{12}}, \frac{\partial f^I}{\partial \sigma_{23}}, \frac{\partial f^I}{\partial \sigma_{13}}\right]^T \tag{9}$$

$$A = -\frac{1}{d\lambda}\frac{\partial f^I}{\partial \kappa} d\kappa. \tag{10}$$

The scalar function A depends on the hardening law. If the hardening parameter κ can be written as a function of the plastic strains,

$$\kappa = \kappa(\varepsilon^{pl}), \tag{11}$$

the differentiated form is:

$$d\kappa = \frac{\partial \kappa}{\partial \varepsilon^{pl}} d\varepsilon^{pl}. \tag{12}$$

Substituting Eq. (12) into Eq. (9) and replacing $d\varepsilon^{pl}$, A can be obtained as

$$A = -\frac{\partial f^I}{\partial \kappa}\frac{\partial \kappa}{\partial \varepsilon^{pl}}\frac{\partial G^I}{\partial \sigma} = -\frac{\partial f^I}{\partial \kappa}\frac{\partial \kappa}{\partial \varepsilon^{pl}}\beta, \tag{13}$$

where

$$\beta = \frac{\partial G^I}{\partial \sigma} = \left[\frac{\partial G^I}{\partial \sigma_{11}}, \frac{\partial G^I}{\partial \sigma_{22}}, \frac{\partial G^I}{\partial \sigma_{33}}, \frac{\partial G^I}{\partial \sigma_{12}}, \frac{\partial G^I}{\partial \sigma_{23}}, \frac{\partial G^I}{\partial \sigma_{13}}\right]^T. \tag{14}$$

If time-dependent effects are taken into consideration, and only yielding (hardening) mechanism I is active, the total strain increment can be decomposed into elastic, plastic and creep strains as:

$$d\varepsilon = d\varepsilon^e + d\varepsilon^{pl} + d\varepsilon^{cr} = D^{-1} d\sigma + d\lambda \frac{\partial G^I}{\partial \sigma} + d\varepsilon^{cr}, \tag{15}$$

where D is the elastic stiffness matrix. Multiplying the both sides of Eq. (15) with $\alpha^T D$ gives

$$\alpha^T D(d\varepsilon - d\varepsilon^{cr}) = \alpha^T d\sigma + \alpha^T D\beta\, d\lambda. \tag{16}$$

Due to Eq. (8), $\alpha^T d\sigma$ at the right-hand side can be replaced by $A\, d\lambda$ resulting in

$$\alpha^T D(d\varepsilon - d\varepsilon^{cr}) = A\, d\lambda + \alpha^T D\beta\, d\lambda. \tag{17}$$

Thus, the factor of proportionality is obtained as

$$d\lambda = \frac{\alpha^T D(d\varepsilon - d\varepsilon^{cr})}{A + \alpha^T D\beta}. \tag{18}$$

2.3. Representation of creep processes

For the Drucker-Prager-Cap model, two types of creep laws are defined in ABAQUS: consolidation creep and cohesion creep [20]. In this investigation, only the consolidation creep mechanism is taken into account. This seems justified since pebble beds in fusion reactors are mainly in a tri-axial compression stress state. For consolidation creep, the creep potential is equal to the plastic flow potential, Eq. (5), of the cap yield surface, i.e.

$$G_c^{cr} = \sqrt{(p - p_a)^2 + (Rq)^2}. \tag{19}$$

The corresponding creep flow rule is given by

$$\mathrm{d}\varepsilon^{\mathrm{cr}} = \frac{\mathrm{d}\bar{\varepsilon}^{\mathrm{cr}}}{f^{\mathrm{cr}}} \frac{\partial G_{\mathrm{c}}^{\mathrm{cr}}}{\partial \sigma}. \tag{20}$$

Here, $\mathrm{d}\varepsilon^{\mathrm{cr}}$ is the work conjugate to the stress tensor σ. The work conjugate of the equivalent consolidation creep stain $\mathrm{d}\bar{\varepsilon}^{\mathrm{cr}}$ is denoted by $\bar{\sigma}^{\mathrm{cr}}$. Thus, f^{cr} is a proportionality factor defined as

$$f^{\mathrm{cr}} = \frac{1}{\bar{\sigma}^{\mathrm{cr}}} \sigma : \frac{\partial G_{\mathrm{c}}^{\mathrm{cr}}}{\partial \sigma}. \tag{21}$$

Buhler [13] has used a strain hardening formulation for the creep law reading in integrated form of equivalent consolidation creep stain $\mathrm{d}\bar{\varepsilon}^{\mathrm{cr}}$ as:

$$\Delta\bar{\varepsilon}^{\mathrm{cr}} = \left[\left(\frac{1}{m} A^{*} \exp\left(-\frac{B}{T} \right) p^{n} \right)^{1/m} \Delta t + \left(\bar{\varepsilon}^{\mathrm{cr},0} \right)^{1/m} \right]^{m} - \bar{\varepsilon}^{\mathrm{cr},0}, \tag{22}$$

where p is the hydrostatic pressure, $\bar{\varepsilon}^{\mathrm{cr},0}$ the creep strain at the beginning of the time step Δt, and A^{*}, B, m, n are material parameters to be obtained from the experimental results.

In ABAQUS, consolidation creep occurs for stress states inside the area between the cap yield surface F_{c} and the critical line $p = p_{\mathrm{a}}$ (see Fig. 2). This means the condition for starting consolidation creep is $p > p_{\mathrm{a}}$. Furthermore, in the "*CAP CREEP" option, the driving force for creep, i.e. the effective creep pressure is defined as $\bar{\sigma}^{\mathrm{cr}} = \bar{p}^{\mathrm{cr}} = p - p_{\mathrm{a}}$, providing a smooth transition to the areas in which consolidation creep in not active ($p < p_{\mathrm{a}}$). For the purpose of this work, the ABAQUS consolidation creep option is not sufficient for the following reason: while the creep strain increases, by the hardening law $p_{\mathrm{b}}(\varepsilon_{\mathrm{vol}}^{\mathrm{in}})$, the value of p_{a} will increase simultaneously. For creep under constant hydrostatic pressure p, this means that the driving force $\bar{p}^{\mathrm{cr}} = p - p_{\mathrm{a}}$ will vanish gradually and, eventually, creep will be stopped. For instance, the starting point of the creep calculation locates inside the cap yield surface, once the creep strains are increasing the cap surface will be moved by the hardening effects of material until the critical line $p = p_{\mathrm{a}}$ surpasses the starting point, which terminates the increasing of creep strains. One possible modification is to define the hardening law as $p_{\mathrm{b}}(\varepsilon_{\mathrm{vol}}^{\mathrm{pl}})$, which totally avoids any hardening effects introduced by creep strains. However, in two step creep experiments [21], the compressive stress is applied in two different steps at the same bed temperature, showing that hardening behaviour may also be introduced by creep strains. The selection of the types of the hardening law depends on the amount of volumetric creep strains present in the material under consideration. For materials with a small range of creep strains, the original ABAQUS definition is sufficient. If there are large creep strain amplitudes, the modification based on $p_{\mathrm{b}}(\varepsilon_{\mathrm{vol}}^{\mathrm{pl}})$ is necessary to obtain correspondingly larger values of the creep strains.

2.4. Other thermo-mechanical material properties

The thermal conductivity of pebble beds is related to the contact areas between particles, which depend on the current stress–strain state. Experiments have been carried out to measure of thermal conductivity of beryllium pebble beds [4,22] and ceramic breeder pebble beds [23]. It is found that the thermal conductivity of beryllium pebble beds changes significantly between un-compacted and compacted pebble beds. This change has a notable impact on the thermo-mechanical analysis. It gives rise to a full (and non-linear) thermo-mechanical two-way-coupling, excluding the classical staggered approach of first solving the thermal boundary value problem and then in a second step computing mechanical equilibrium for the obtained thermal strains. So, it is essential to model the material behaviour with respect to the change of thermal conductivity. By systematical experimental investigation on the thermal conductivity of pebble beds under different compressive strains and temperatures [4], an empirical equation describing the strain dependent thermal conductivity is obtained:

$$\begin{aligned} k(\mathrm{W/(m\,K)}) = {} & 1.81 + 0.0012T\,(^{\circ}\mathrm{C}) - 5 \\ & \times 10^{-7} T\,(^{\circ}\mathrm{C})^{2} + (9.03 - 1.386 \\ & \times 10^{-3} T\,(^{\circ}\mathrm{C}) - 7.6 \times 10^{-6} T\,(^{\circ}C)^{2} \\ & + 2.1 \times 10^{-9} T\,(^{\circ}C)^{3}) \varepsilon\,(\%) \end{aligned} \tag{23}$$

The functional form of Eq. (23) is adopted from the semi-empirical Schluender–Bauer–Zehner (SZB) model and the coefficients are identified from experiments. It has been determined for bed temperatures

between 200 and 650 °C and for a maximum pebble bed deformation of 3.5%.

Eq. (23) makes a fully coupled thermo-mechanical analysis necessary, as the change of deformation has a strong influence on the thermal conductivity and, thus, on the temperature field. The volumetric inelastic strain-dependent thermal conductivity $k(\varepsilon^{\text{in}}_{\text{vol}}, T)$ found in experiments, which is represented by Eq. (23), has been implemented in ABAUQS by a USDFLD routine.

Furthermore, the coefficient of thermal expansion and the specific heat for the different materials [15], which have been obtained from experiments, have been implemented in ABAQUS as functions of temperature.

3. Determination of material parameters

The present model describes the thermo-mechanical properties of pebble beds in terms of non-linear elasticity, plasticity, time-dependent effects and the thermal-mechanical interactions by a multi-parameter system. The only available experimental basis for the determination of the material parameters is the oedometric test, which is not a strictly proportional stress loading. Therefore, it is necessary to find relations between the experiments and the material parameters in the constitutive model. In this section, such relations and the determination of the material parameters in present model are discussed and some validations are shown in Section 4. With the present method the relation between the hardening law and experimental results can be determined uniquely, and no try-and-error method is necessary. This method is mainly based on the analysis of the stress–strain state of oedometric compression experiments, therefore, the experiments will be introduced first.

3.1. Oedometric compression experiments

The oedometric compression test (see Fig. 3) is one of the basic experimental setups for characterizing the properties of granular materials, such as soil and sand. In Fig. 3, the loading force F_y and the displacement of the pressure plate represent the overall stress and strain states in the experiments. On the other hand, in oedometric compression experiments, the walls around specimens are fixed in the oedometric test. In contrast to uniaxial compression or hydrostatic compression, this

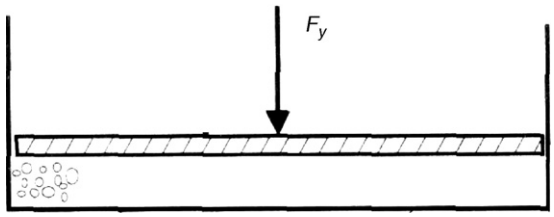

Fig. 3. A sketch of oedometric compression experiments.

means a combination of stress and strain boundary conditions. The experimental investigation for the ceramic breeder and beryllium pebble beds has been performed by FZK [16,18,24]. The analysis of the stress state of oedometric compression will be discussed later.

Oedometric tests are carried out for various temperature levels, starting from room temperature to 900 °C for Li_4SiO_4 and 480 °C for beryllium pebble beds. The loading and unloading branches of the stress–strain curves are represented by separate temperature dependent empirical fit functions, the so-called Reimann fits:

$$\begin{aligned}\sigma^{\text{L}} &= [C^{\text{L}}_1(C^{\text{L}}_2 + C^{\text{L}}_3 T^{C^{\text{L}}_4})\varepsilon]^{1/1-C^{\text{L}}_5}\\ \sigma^{\text{U}} &= [C^{\text{U}}_1(C^{\text{U}}_2 + C^{\text{U}}_3 T^{C^{\text{U}}_4})\varepsilon]^{1/1-C^{\text{U}}_5}\end{aligned}. \tag{24}$$

Superscripts L and U indicate the loading and unloading branches. For each material, parameters C^{L}_i and C^{U}_i are chosen such to yield optimum representation of the experimental loading and unloading curves.

Also, results of a few biaxial compression experiments can be found in the literature [25]. While usually the pebble beds are under triaxial compression in working conditions, triaxial results are difficult to be obtained in experiments. Therefore, the material model will have to be developed based on available experimental data.

3.2. Deformation mechanism of oedometric experiments

The stress state of the oedometric compression experiments, Fig. 3, can be sketched as Fig. 4. Since, $\sigma_x = \sigma_z$, the problem is reduced to an axisymmetric one. Here, q and p are given by:

$$\begin{aligned}q &= |\sigma_y - \sigma_x|\\ p &= -\frac{\sigma_y + 2\sigma_x}{3}\end{aligned}. \tag{25}$$

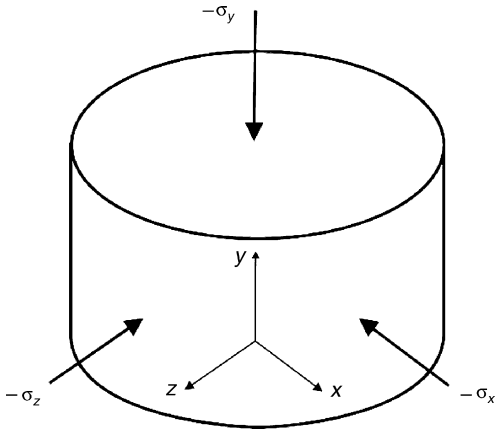

Fig. 4. The stress state of oedometric experiments (Hofer and Kamlah [1]).

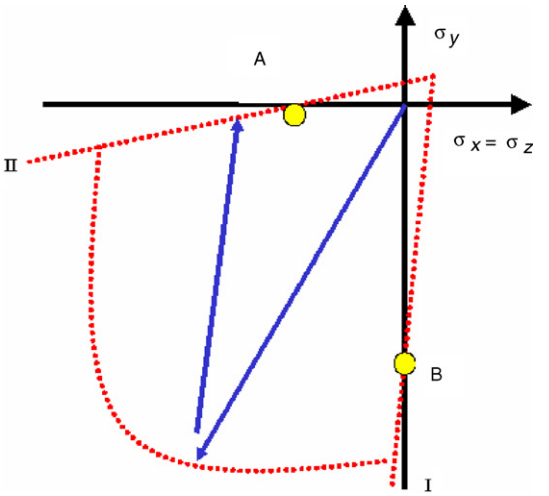

Fig. 5. A sketch of the loading and unloading path of oedometric experiments in the σ_y–σ_x plane.

As the material deforms elastically, the following relations can be obtained by the theory of isotropic elasticity:

$$\sigma_x = \sigma_z = \frac{\nu}{1-\nu}\sigma_y, \tag{26}$$

$$\sigma_y = \frac{1-\nu}{(1+\nu)(1-2\nu)}E\varepsilon_y. \tag{27}$$

With Eq. (26), non-linear Young's modulus, Eq. (1), reads as

$$E = E_0 + A_e\left[\frac{2(1-\nu)}{(1+\nu)(1-2\nu)}\right]^{-s/2}(\sigma_y)^s, \tag{28}$$

The above relation is valid during pure elastic deformation only, since use has been made of the elastic relation in Eq. (26). During elasto-plastic loading, the ratio between axial and lateral stresses is different from the elastic one in Eq. (26), and Eq. (28) needs to be updated. Thus, Eq. (28) is called the "elastic prediction" of Young's modulus in oedometric experiments.

A sketch of the loading and unloading path in the $\sigma_y - \sigma_x$ plane is plotted in Fig. 5. This is an alternative representation of the Drucker-Prager-Cap yield surface valid for the special type of axisymmetric stress states acting in the oedometric test. The dotted line is the yield (failure) surface, transferred to $\sigma_y - \sigma_x$ plane. If during loading in the oedometric test, cap yielding is active, the following equations are satisfied by the yielding criterion and plastic flow potential:

$$\begin{aligned} &F_c = 0 \\ &\left.\frac{\partial G_c}{\partial \sigma_x}\right|_{\sigma_x=\sigma_z} = 0 \end{aligned} \tag{29}$$

The first equation is the cap yield criterion, satisfied while cap yield is active, and the second one is derived from the plastic flow potential by taking into account the condition of rigid side walls in the oedometric test (see Section 2.2.2). During the compression, $\varepsilon_x = \varepsilon_z = 0$ is valid due to the rigid wall condition, but for the increments of plastic strains in the transverse plane, the second equation in Eq. (29) is the approximation to the condition on the total strain.

Expressing this in terms of the principle stresses for the case of axisymmetric loading, and this system of equations can be solved for the hardening parameter p_b as a function of stress component σ_y, giving

$$p_b = -\frac{3\sec^2\beta(\cos\beta + R\sin\beta) \times (-3\cos\beta + \sqrt{4+9R^2}\,\sin\beta)}{-9 + (4+9R^2)\tan^2\beta}\sigma_y. \tag{30}$$

Although Eq. (30) cannot provide the exact definition of hardening law yet, there is possibility to reveal

the relation between compression stress and plastic strain through Reimann fits.

3.3. Reimann fits for loading and unloading

First, we recall the empirical curves by Reimann for the oedometric experiments. While in the unloading branch σ^{U} of Eq. (24), the strain ε represents purely elastic strain changes during unloading, the strain in the loading branch σ^{L} is the sum of the elastic and plastic strain changes during loading. Thus, Eq. (24) can be written as

$$\begin{aligned}\sigma_y^{\mathrm{L}} &= [C_1^{\mathrm{L}}(C_2^{\mathrm{L}} + C_3^{\mathrm{L}} T^{C_4^{\mathrm{L}}})(\varepsilon^{\mathrm{el}} + \varepsilon^{\mathrm{pl}})]^{1/1-C_5^{\mathrm{L}}} \\ \sigma_y^{\mathrm{U}} &= [C_1^{\mathrm{U}}(C_2^{\mathrm{U}} + C_3^{\mathrm{U}} T^{C_4^{\mathrm{U}}})\varepsilon^{\mathrm{el}}]^{1/1-C_5^{\mathrm{U}}}\end{aligned} \quad . \tag{31}$$

Comparing the non-linear Young's modulus in Eq. (28) to the elastic (unloading) part of the Reimann fits Eq. (31), we identify

$$\begin{aligned}&\frac{E_0}{E} \to 0 \\ &s = C_5^{\mathrm{U}} \\ &A_{\mathrm{e}} = 2C_1^{\mathrm{U}}(C_2^{\mathrm{U}} + C_3^{\mathrm{U}} T^{C_4^{\mathrm{U}}}) f(\nu)^{1-s/2} g(\varepsilon_{\mathrm{vol}}^{\mathrm{in}})\end{aligned} \quad , \tag{32}$$

where

$$\begin{aligned}f(\nu) &= \frac{(1+\nu)(1-2\nu)}{2(1-\nu)} \\ g(\varepsilon_{\mathrm{vol}}^{\mathrm{in}}) &= 1 + \frac{\varepsilon_{\mathrm{vol}}^{\mathrm{in}}}{\varepsilon_{\mathrm{vol}}^{\mathrm{in},0}}\end{aligned} \tag{33}$$

In Eq. (32), $g(\varepsilon_{\mathrm{vol}}^{\mathrm{in}})$ is a function to adjust the difference between the elastic prediction according to Eq. (28) and the exact elasto-plastic loading path. Eq. (28) is valid only in pure elastic deformation. Once the material had behaved irreversibly, the ratio of stresses will be different from Eq. (26) even for the case of elastic unloading. The present non-linear elasticity law depends on the stress state, however the elastic prediction is different from the elasto-plastic loading path because of the changing of inelastic strains. The difference in these two stress states is accounted for approximately by the function $g(\varepsilon_{\mathrm{vol}}^{\mathrm{in}})$. Only a first order, i.e. linear functional form of $g(\varepsilon_{\mathrm{vol}}^{\mathrm{in}})$ is taken into account, and the values of $\varepsilon_{\mathrm{vol}}^{\mathrm{in},0}$ are chosen to fit the empirical curves.

Next, we eliminate the elastic strain change in the plastic (loading) part of Eq. (31) by means of the corresponding unloading part and solve for the plastic strain change to obtain

$$\varepsilon^{\mathrm{pl}} = \frac{(\sigma_y)^{1-C_5^{\mathrm{L}}}}{C_1^{\mathrm{L}}(C_2^{\mathrm{L}} + C_3^{\mathrm{L}} T^{C_4^{\mathrm{L}}})} - \frac{(\sigma_y)^{1-C_5^{\mathrm{U}}}}{C_1^{\mathrm{U}}(C_2^{\mathrm{U}} + C_3^{\mathrm{U}} T^{C_4^{\mathrm{U}}})}. \tag{34}$$

Note the dependence on both the C_i^{L} and C_i^{U}.

Combining Eqs. (30) and (34), the hardening law $p_{\mathrm{b}} \sim \varepsilon^{\mathrm{pl}}$ is obtained. To each value of $\varepsilon^{\mathrm{pl}}$, there is related a unique value of p_{b} in analytical form depending on the values of C_i^{L} and C_i^{U} as they are provided by Reimann fits representing the experimental data. So, with the procedure discussed above, the elasto-plastic parameters in the present model can be determined unambiguously from the experimental results without any try-and-error method.

3.4. The advantages of the improvement

There are two main advantages of this improvement. First, it is possible to directly use the empirical Reimann fit equations from the experiments to determine uniquely the set of material parameters, especially the hardening laws, instead of using a try and error method. It turns out that the latter method may deliver various sets representing the oedometric experiment more or less well, however, they may result in totally different and possibly unphysical responses for other loading histories. By the method developed in this work, we identify the right set of parameters.

Second, since this procedure can be carried out for each temperature level, the temperature dependence of the hardening law is introduced into the model in an unambiguous way. This means that the thermo-plastic generalization of the constitutive model for pebble beds is obtained in a straight forward manner from the temperature dependent Reimann fits. Fig. 6 shows a sketch of the yield (failure) surfaces in stresses–temperature–space. In this way, the inelastic response of the material for different temperatures can be predicted. For instance, if the temperature varies, the theory might describe changed yielding behaviour of the material [26].

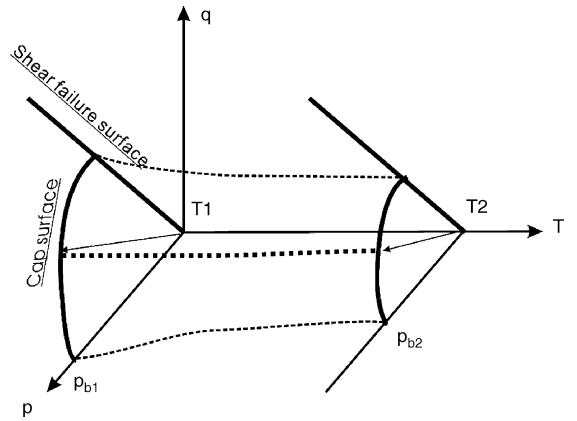

Fig. 6. A sketch of the Drucker-Prager-Cap yielding/failure surfaces of thermoplasticity.

4. Validation and discussion

4.1. Validation for hardening law

For the purpose of validation of the method discussed above, the material data from oedometric compression experiments are needed. Table 1 gives a set of parameters of Reimann fits, Eq. (31), for both breeding ceramics, Li_4SiO_4 and beryllium pebble beds [15].

For beryllium pebble beds, the Poisson ratio $\nu = 0.05$, and for Li_4SiO_4 breeder pebble beds, $\nu = 0.25$ [27]. The procedure of determining the material parameters has been implemented in a USDFLD routine.

$$F_s = q - p\tan\beta - d = 0 \Rightarrow \begin{matrix} \mathrm{I}: \sigma_x - \sigma_y + \dfrac{1}{3}(\sigma_y + 2\sigma_x)\tan\beta - d = 0 \\ \mathrm{II}: \sigma_y - \sigma_x + \dfrac{1}{3}(\sigma_y + 2\sigma_x)\tan\beta - d = 0 \end{matrix}, \quad (35)$$

And for beryllium pebble beds, we take $\varepsilon_{\mathrm{vol}}^{\mathrm{in},0} = 0.02$, and for Li_4SiO_4 breeder pebble beds, $\varepsilon_{\mathrm{vol}}^{\mathrm{in},0} = 0.05$ is used. As validation, we simulate the oedometric experiment with the present model and compare the predicted results with the experiments. Fig. 7 presents the comparison between the present FEM model and the experiments for both ceramic breeder pebble beds and beryllium pebble beds. The FEM results include an unloading and reloading path at 3 MPa. Fig. 7 shows a good agreement of the prediction by the model with the empirical curves during both loading and unloading branches. This validation proves the accuracy of the method discussed above to determine the material parameters of both elasticity and plasticity in the present model.

Table 1
The parameters of "Reimann fits" for oedometric compression

i	Li_4SiO_4		Beryllium	
	C_i^{L}	C_i^{U}	C_i^{L}	C_i^{U}
1	154.0	170.0	154.0	870.0
2	1.0	1.0	1.0	1.0
3	−8.5E−10	−8.5E−10	0.0	0.0
4	3.0	3.0	1.0	1.0
5	0.47	0.60	0.586	0.65

4.2. The softening behaviour in the previous model

In the previous material modelling [1], the Drucker-Prager friction angle has been chosen as 45°. Unrealistic plastic softening behaviour was observed in the model when simulating unloading in the oedometric test to zero stresses resulting in an almost complete vanishing of the plastic strains. Fig. 8 shows the stress–strain curves for different values of the Drucker-Prager friction angle β (40–60°). The smaller the β value, the more pronounced softening behaviour is found. In Fig. 5, the slopes of the shear failure surfaces are defined by β. For axisymmetric conditions, the shear failure surface can be transformed from the q–p plane to the σ_y–σ_x plane as

where "I" and "II" refer to the shear surfaces in the σ_y–σ_x plane, respectively, see Fig. 5. Thus, we may obtain the coordinates of the intersections (A and B) between the shear failure surfaces and the σ_y- and σ_x-axes. We get

$$\begin{matrix} A: \left(-\dfrac{d}{1 - 2/3\tan\beta}, 0\right) \\ B: \left(0, -\dfrac{d}{1 - 1/3\tan\beta}\right) \end{matrix}. \quad (36)$$

For a relatively small d, as in the case of pebble beds, intersection A is close to the origin point of the σ_y–σ_x

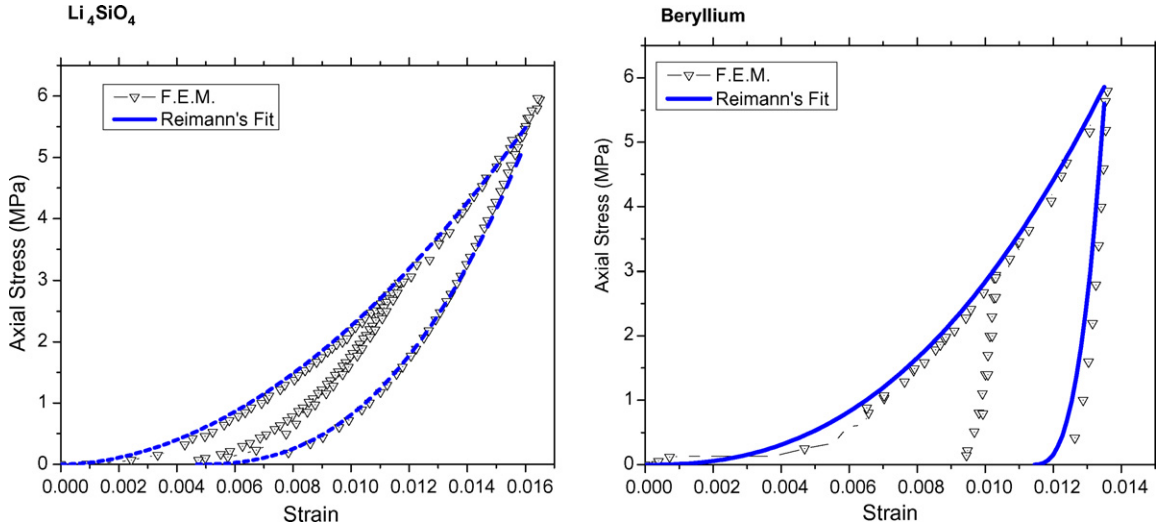

Fig. 7. The prediction of the present model compared with the experimental fits (parameters from Fokkens [15]): *left*, ceramic breeder pebble beds; *right*, beryllium pebble beds.

plane. Consequently, the main reason for the softening behaviour while unloading is that the failure surface is hit before complete unloading to zero compressive stresses has occurred. If the unrealistic softening during unloading is to be avoided, the shear failure surface "II" should be parallel to the σ_x-axis or have an intersection for $\sigma_x > 0$. This means a condition for the slope, i.e., β, and, by Eq. (36), we find

$$\tan\beta \geq 1.5. \tag{37}$$

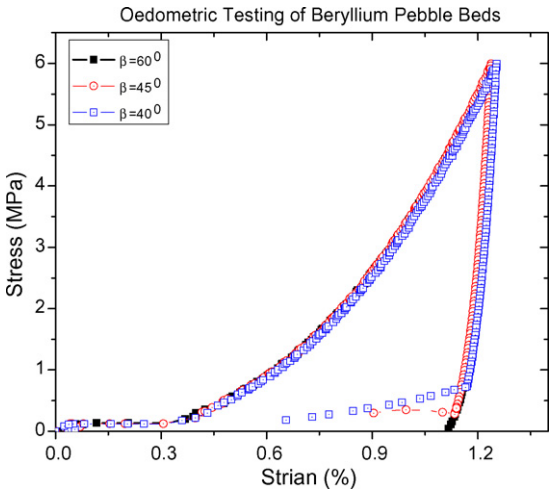

Fig. 8. The effects of β on the softening behaviours while unloading.

As mentioned above, for a small value of β, the unloading path will hit the shear failure surface before the axial stress is reduced to zero, initiating the unrealistic softening behaviour during final unloading, while Eq. (37) provides the condition to avoid such behaviour.

Note that the Drucker-Prager friction angle β is not identical to the friction angle of granular materials, but it is a function of the real friction angle. The Drucker-Prager friction angle β can be estimated by the Leonardo da Vinci's static friction experiment for a granular medium, see Fig. 9 [28]. The static friction coefficient is defined as

$$\mu_s = \frac{T}{P} = \frac{\tau}{\sigma_n}. \tag{38}$$

The three-dimensional stress state in the static friction experiment is shown in Fig. 9 (right). The stresses on the cubic element represent the stress state in the sheared middle layer of the experimental setup. By analyzing the stress state in the middle layer, it is found that the middle layer of the static friction experiment is in a similar stress state as the pebble bed in the oedometric test. The normal stresses in the transverse plane are determined by the effect of the Poisson ratio and a condition of axisymmetric symmetry in this plane. Consequently, the stress tensor can be

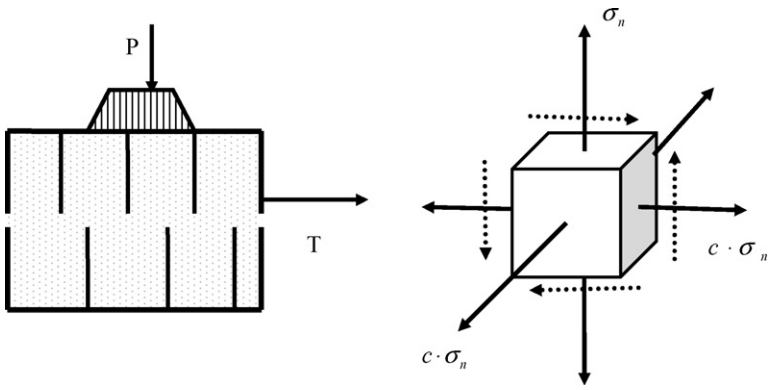

Fig. 9. *Left*, A sketch of typical experimental setup used to measure the coefficient of the static friction μ_s of a granular material; *right*, the stress state in the sheared middle layer of the setup to the left.

expressed as

$$\begin{pmatrix} \sigma_n & \tau & 0 \\ \tau & c\sigma_n & 0 \\ 0 & 0 & c\sigma_n \end{pmatrix}. \tag{39}$$

In this stress tensor, the stress ratio $c = \nu^*/(1-\nu^*)$ depends on the kind of loading. For pure elastic deformation, $\nu^* = \nu$ is the elastic Poisson ratio, Eq. (26). In the case of elastic–plastic deformation, $\nu^* = \nu^{pl}$ is some history dependent quantity with a value in the range $0 \le \nu^{pl} \le 0.5$. Expressing this stress state in Drucker-Prager-Cap theory as

$$q = \sqrt{\left(\frac{1-2\nu^*}{1-\nu^*}\sigma_n\right)^2 + 3\tau^2}, \qquad p = \frac{1+\nu^*}{3(1-\nu^*)}\sigma_n \tag{40}$$

we have

$$\tan\beta = 3\frac{\sqrt{(1-2\nu^*)^2 + 3\mu_s^2(1-\nu^*)^2}}{1+\nu^*}. \tag{41}$$

Here, the Drucker-Prager friction angle β is expressed as a function of the static friction coefficient μ_s and the Poisson ratio ν^* ($=\nu$ or $=\nu^{pl}$), see Fig. 10. The value of β is a monotone function of μ_s for $\mu_s \ge 0$.

The value of μ_s can be obtained by several kinds of experiments, and on the basis of μ_s, a rough range of the Drucker-Prager friction angle can be estimated. For the shear failure surface to be parallel to the $\sigma_x = \sigma_z$-axis, the condition $\tan\beta = 1.5$ has to be satisfied (see Fig. 5 and Eq. (37)). By solving Eq. (41), and considering the extreme condition $\mu_s = 0$ for a totally non-friction material, $\nu^* \le \nu_0 = 0.2$ guarantees that the unloading path will not hit the shear failure surface. With lager values of μ_s, the critical value of Poisson ratio ν_0 increases, for instance, $\nu_0 = 0.5$ while $\mu_s \ge \sqrt{3}/2$. By Eq. (41), the region satisfying $\tan\beta \ge 1.5$ can be found in Fig. 10.

According to the available bi-axial experimental data for ceramic breeder pebble beds ([25] and "*Material Assessment Report*" for ITER), the Drucker-Prager friction angles of the pebble beds can be calculated by analyzing the stress state in bi-axial compression.

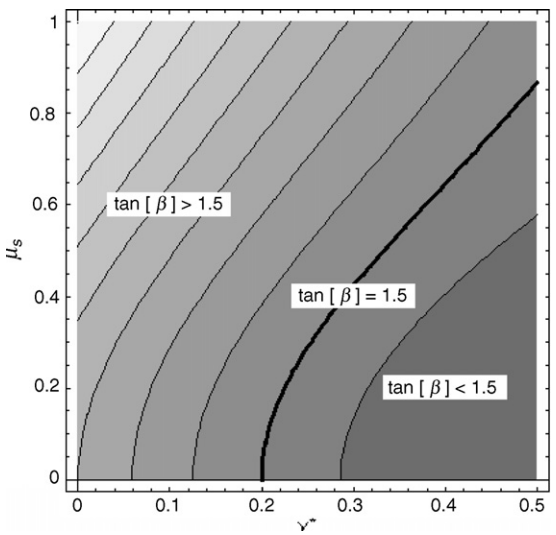

Fig. 10. $\tan\beta$ as a function of the static friction coefficient μ_s and the Poisson ratio ν^*, the bolded line shows the critical value of $\tan\beta$.

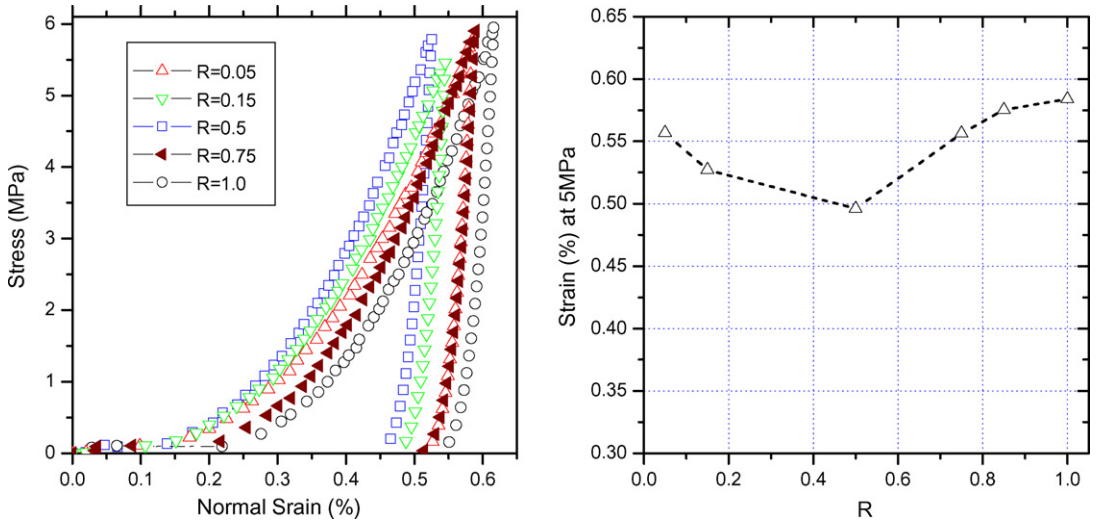

Fig. 11. The hydrostatic compression with different values of R: *left*, stress–strain curves; *right*, strains at 5 MPa with different R-values.

Following Eq. (35) for shear failure surface "I" in the axisymmetric stress plane, and assuming $d = 0$ for simplicity, we have:

$$\tan\beta = \frac{3(\sigma_y^0 - \sigma_x^0)}{\sigma_y^0 + 2\sigma_x^0}. \tag{42}$$

Superscript 0 indicates the failure stress in experiments. As a result, values of almost around 60° are found for the Drucker-Prager friction angle β of both ceramic breeder and beryllium pebble beds. As discussed above, such a value is in accordance with the criterion for avoiding unrealistic softening, i.e. Eq. (37). Consequently, both the experimental results and theoretical considerations of the Drucker-Prager theory support the choice of the Drucker-Prager friction angle $\beta \approx 60°$. On the other hand, as shown before, for such a value no unreasonable plastic softening behaviour occurs in the model.

4.3. Sensitivity of constitutive model with respect to material parameter R

Most of the material parameters can be determined by the method presented above from with the empirical equations of the Reimann fits. However, some parameters are adjusted "manually", i.e. by try and error, which does not effect the predictions in oedometric test but possibly in other loading paths. In principle, these parameters can be determined by experiments employing different loading paths, such as hydrostatic compression or triaxial compression. Fig. 11 shows the impact of R on the simulation of hydrostatic compression. In Fig. 11, the left plot shows the stress–strain curves and the right plot is the normal strain at 5 MPa versus the corresponding value of the parameter R.

Only the determination of the value of R is missing in the present model. This constant controls the shape of cap surface, and mainly effects the direction of the plastic and creep flows. However, Fig. 11 clearly shows that the stress–strain curves are not very sensitive to variations of R over a wide range. From the current point of view, these findings indicate that tremendous efforts for experiments with new type of loading states in order to identify R exactly seem not to be justified. Instead, some reasonable estimate for R will be sufficient for the purposes of this work.

4.4. Creep properties

In addition, creep experiments have been performed and empirical creep equations were obtained [19] of the type:

$$\varepsilon^{\mathrm{cr}} = A \exp\left(-\frac{B}{T}\right) \sigma^n t^m \tag{43}$$

Parameters A, B, n, m have been determined by experiments for different materials, such as ceramic

Table 2
The parameters for the creep experiments (units: MPa/s/K)

	Li_4SiO_4	Beryllium
A	12.12	3.874
B	10220.0	9124.0
n	0.65	0.62
m	0.2	0.35

breeder and beryllium pebble beds. The parameters of Li_4SiO_4 and beryllium pebble beds are listed in Table 2 [17,19].

In view of the discussing in Section 2.3, the parameters (A^*, B, m, n) in Eq. (22) can be identified from experiments for different materials. It has been reported that due to a bug the "strain hardening" form of consolidation creep is not available in ABAQUS in analyses of two-step creep [1]. The consolidation creep has been re-implemented in ABAQUS by a CREEP routine. In contrast to the ABAQUS formulation reported in Section 2.3, in this investigation, the effective creep pressure $\bar{p}^{cr}$ is taken to be equal to the total hydrostatic pressure p at the current stress state. By this approach, the fit equations for the experimental data [19] can be used directly in the formulation of consolidation creep. Eq. (43) is formulated in term of uniaxial stress σ, whereas Eq. (22) for the consolidation creep relies on hydrostatic pressure p. This difference is taken into account by the ratio A^*/A, while the other parameters (B, m, n) are the same in both cases. In order to minimize the difference between the predictions of the model and experiments, we choose for A^*/A the value of 2.2 for both Li_4SiO_4 and beryllium pebble beds.

The validation of the creep modelling has been made for different compression stresses and bed temperatures of Li_4SiO_4 and beryllium pebble beds, respectively. Fig. 12 shows a comparison between the prediction of model and the experimental results. Two typical examples for single step stress loading are given with the maximum creep strain up to 3% (Li_4SiO_4 at 2.2 MPa and 850 °C as well as 6.5 MPa and 650 °C) and 2% (beryllium at 1.7 MPa and 635 °C as well as 1.7 MPa and 635 °C). It can be seen that the identification of the material constants has been successful. The two-step creep experiment of beryllium pebble beds in Fig. 13 may serve as an independent validation experiment, since such a loading history was not the basis of the identification of the creep parameters. The comparison shows that present model is well capable of representing the creep processes in the pebble beds considered here.

In additional, the relations between parameters in current material model and experimental results are listed briefly in Table 3, in order to give an overview of the present method. C_i^L and C_i^U are the coefficients of "Reimann fits" for oedometric compression, which can be found in Table 1.

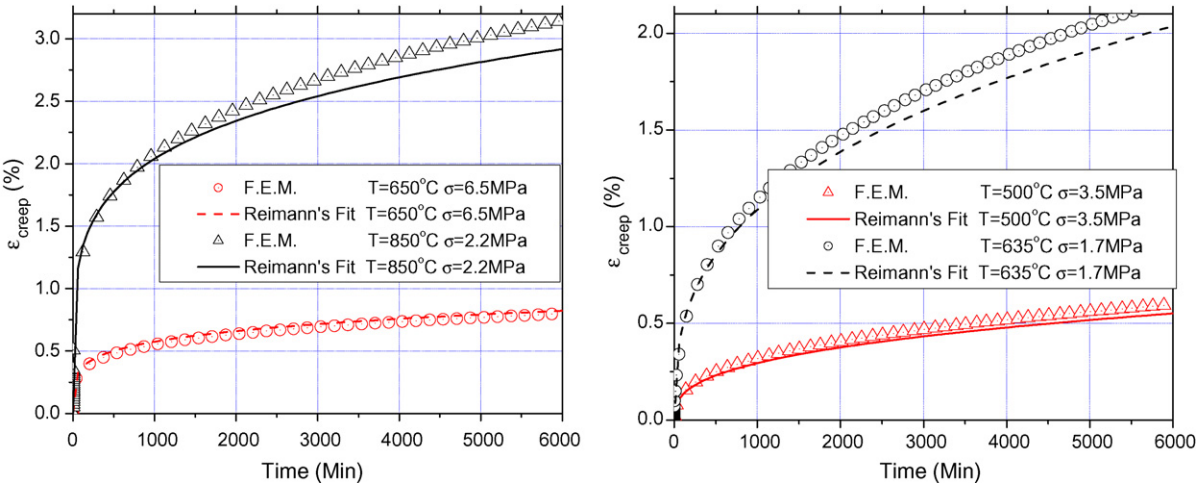

Fig. 12. The creep prediction of the present model compared with experimental fits (Reimann and Worner [19]; Reimann and Harsch [17]): *left*, ceramic breeder pebble beds; *right*, beryllium pebble beds.

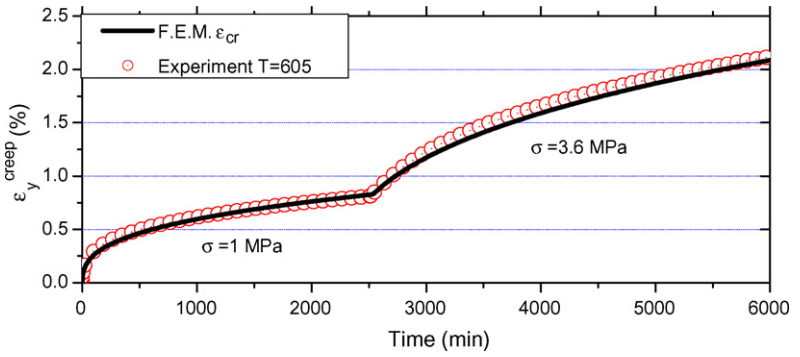

Fig. 13. The two-step creep experiment, the comparison of the prediction of the present model and experiment ($T = 605\,^{\circ}C$ [4]).

4.5. Application to pebble beds assembly (PBA)

For the validation purpose, the analysis of the pre-compaction procedure of the pebble bed assembly (PBA) capsule used for experiments in the HFR reactor at NRG Petten is carried out. This procedure has been analyzed in detail by Fokkens [15] with the assumption that the pebble beds have two different elastic laws while loading and unloading. The geometric model of PBA is sketched in Fig. 14. Ceramic breeder and beryllium pebble beds are included in PBA. The compression stress σ is applied on the pressure lid, and cycles at the first mechanical loading with the temperature at 20 °C. In the first 37.5 s, the pressure increases and decreases at rate of 0.4 MPa/s, and the maximum pressures are 1, 2, 3 MPa at every loading cycle in 30 s, and then reloads to 3 MPa. Second, thermal loading, the temperature of PBA is raised uniformly to 350 °C at rate 0.04 °C/s under the constant pressure 3 MPa; then the whole PBA keeps the constant pressure and temperature for 24 h; and finally thermal unloading to 20 °C at rate 0.04 °C/s and mechanical unloading at rate 0.4 MPa/s [15]. This calculation has been carried out for the case of uniformly heating to find out the influence of volumetric inelastic strain on the thermal conductivity of beryllium pebble beds. This influence has been investigated by experiments [4,22,23], suggesting

Table 3
The summary of material parameters used in this paper

Parameters in model	Expressed by experimental results
Non-linear elasticity	
A_e	Eq. (32)
s	C_5^U
ν	0.05 for beryllium and 0.25 for Li_4SiO_4 pebbles [27]
E_0	~0
Drucker-Prager-Cap theory	
R	0.9
β	60° [25]
p_b	Eqs. (30) and (34)
d	~0
Creep law	
A, B, m, n	Experimental coefficients in Eq. (43), i.e. Table 2 [17,19]

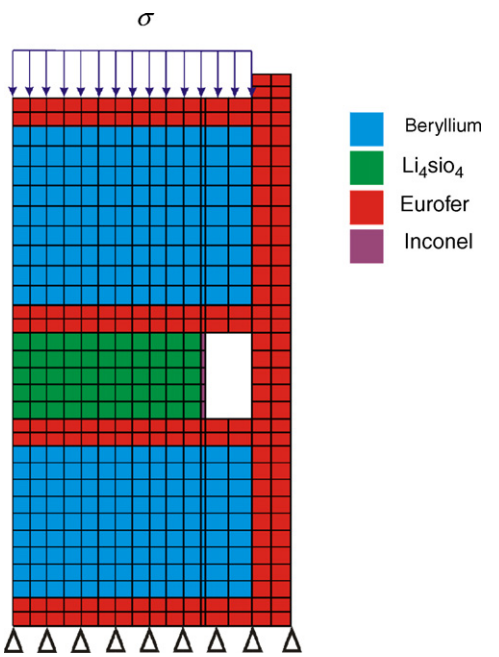

Fig. 14. A sketch of the axisymmetric finite element model of pebble bed assembly (PBA).

that the one of beryllium pebble beds is more significant than ceramics breeder pebble beds, and should be taken into account for the thermal–mechanical coupled analysis.

Using the modified Drucker-Prager-Cap model with the present identification method of material parameters, the pre-compaction procedure has been analyzed. The stress–displacement curve on the pressure lid is shown in Fig. 15, and the result obtained by Fokkens [15] is plotted inside for comparison. The result shows that the present model works well in the thermo-mechanically coupled finite element analysis.

With the implementation of the strain-dependent thermal conductivity in USDFLD, the profile of the thermal conductivity of beryllium pebble beds can be predicted by the present material model (see Fig. 16). The thermal conductivity has been modelled as a function of both volumetric inelastic strain and temperature, as Eq. (23). The magnitudes of thermal conductivity

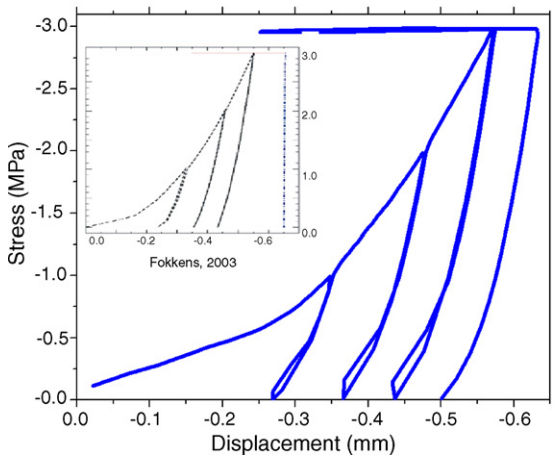

Fig. 15. The stress–displacement curve of the pressure lid during the entire pre-compaction procedure, small plot is the results from Fokkens [15].

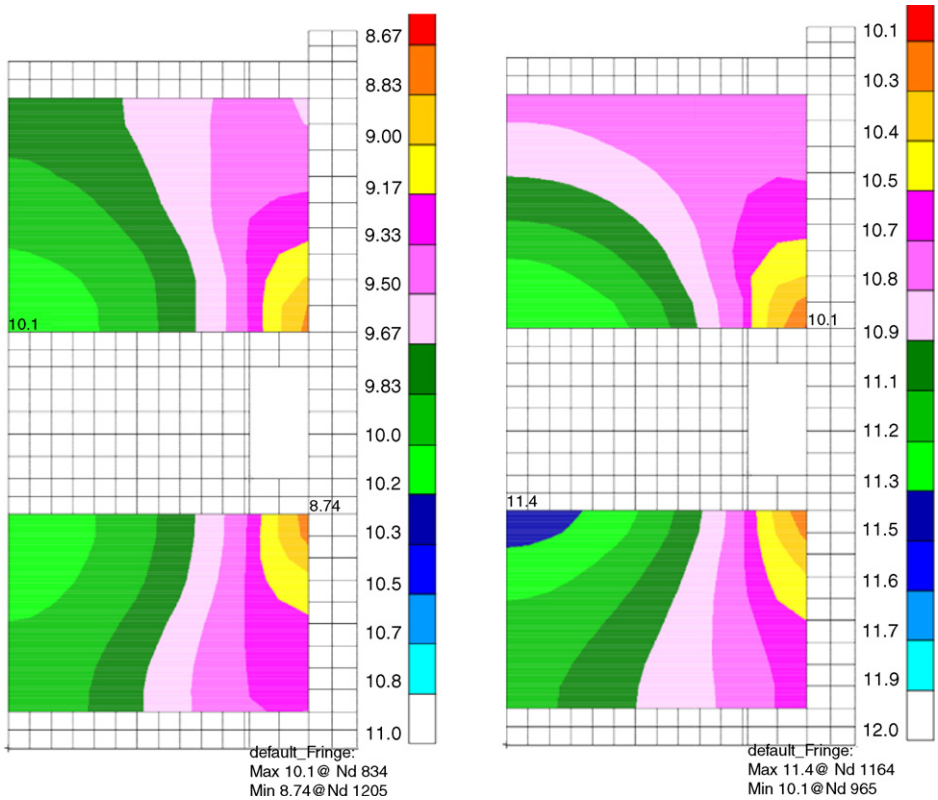

Fig. 16. Thermal conductivity (W/m °C) profile of beryllium pebble beds: (*left*) after the mechanical cycling; (*right*) after the pre-compaction procedure.

are 8.74–10.1 W/m °C after the mechanical cycling and 10.1–11.4 W/m °C after the total pre-compaction analysis, compared with the value without any inelastic strains in the material (about 2 W/m °C) at the beginning of the procedure.

5. Conclusion

In this paper, the thermo-mechanical properties of ceramic breeder and beryllium pebble beds are investigated. Because the pebble size is sufficiently small compared with the bed dimensions, a continuum mechanics approach is used for the thermo-mechanical modelling of pebble beds. Motivated by the results of experimental investigations, the present material model is mainly composed of a non-linear elasticity law, the Drucker-Prager-Cap theory, a modified consolidation creep law and a volumetric inelastic strain-dependent thermal conductivity. The present material model can be applied in fully coupled thermo-mechanical finite element analysis for pebble beds.

To determine the material parameters in the present model, a method is proposed to find the proper set of material parameters from the available experiments. This method is based on the analysis of the deformation in the oedometric test, which is the basic experimental setup for characterizing the material properties of pebble beds. The hardening law of the Drucker-Prager-Cap theory is identified through empirical equations (Reimann fits) representing the experimental data. Validation of the material model of both ceramic breeder and beryllium pebble beds shows that the predictions of model agree well with the experimental results.

Furthermore, the thermo-mechanical model developed in this work is applied to the analysis of the precompaction procedure of the pebble bed assembly (PBA) capsule used for experiments in the HFR reactor at NRG Petten.

Acknowledgements

This work, supported by the European Communities under the contract of Association between EURATOM and Forschungszentrum Karlsruhe, was carried out within the framework of the European Fusion Development Agreement. The views and opinions expressed herein do not necessarily reflect those of the European Commission.

References

[1] D. Hofer, M. Kamlah, Drucker-Prager-Cap creep modelling of pebble beds in fusion blankets, Fusion Eng. Des. 73 (2005) 105–117.
[2] O. Coube, Modelling and numerical simulation of powder die compaction with consideration of cracking, PhD Thesis, University Pierre et Marie, Paris VI, 1998.
[3] ABAQUS, Analysis User's Manual, Version 6.5, 2004.
[4] J. Reimann, G. Piazza, Z. Xu, A. Goraieb, H. Harsch, Measurements of the thermal conductivity of compressed beryllium pebble beds, FZKA 7096 (2005).
[5] L.V. Boccaccini, N. Bekris, Y. Chen, U. Fischer, S. Gordeev, S. Hermsmeyer, E. Hutter, K. Kleefeldt, S. Malang, K. Schleisiek, I. Schmuck, H. Schnauder, H. Tsige-Tamirat, Design description and performance analyses of the European HCPB test blanket system in ITER feat, Fusion Eng. Des. 61–62 (2002) 339–344.
[6] S. Hermsmeyer, B. Dolensky, J. Fiek, U. Fischer, C. Koehly, S. Malang, P. Pereslavtsev, J. Rey, Z. Xu, Revision of the EU Heilium cooled pebble bed blanket for DEMO, in: Proceedings of the SOFE Conference, San Diego, 2003.
[7] J. Reimann, L. Boccaccini, M. Enoeda, A.Y. Ying, Thermomechanics of solid breeder and Be pebble bed materials, Fusion Eng. Des. 61–62 (2002) 319–331.
[8] Z. Lu, A.Y. Ying, M.A. Abdou, Numerical and experimental prediction of the thermomechanical performance of pebble beds for solid breeder blanket, Fusion Eng. Des. 49 (2000) 605–611.
[9] A. Ying, H.L. Huang, M. Abdou, Numerical simulation of ceramic breeder pebble bed thermal creep behavior, J. Nucl. Mater. 307 (2002) 827–831.
[10] D. Aquaro, Thermal mechanical analysis of a solid breeding blanket, Fusion Eng. Des. 69 (2003) 511–518.
[11] D. Aquaro, N. Zaccari, Experimental and numerical analysis on pebble beds used in an ITER Test Module Blanket, Fusion Eng. Des. 81 (2006) 707–712.
[12] D. Aquaro, N. Zaccari, Pebble bed thermal–mechanical theoretical model—application at the geometry of test blanket module of ITER-FEAT nuclear fusion reactor, Fusion Eng. Des. 75–79 (2005) 903–909.
[13] L. Buhler, Coninuum models for pebble beds in fusion blankets, FZKA 6561 (2002).
[14] P.A. Di Maio, E. Oliveri, G. Vella, Fusion Pebble Bed Thermo-Mechanical Modelling Final Report A–C, Dipartimento di Ingegneria Nucleare, Universita degli studi di Palermo, Italy, 2002.
[15] J.H. Fokkens, Thermo-mechanical finite element analysis of the HCPB in-pile test element, NRG Report 21477/02.50560/P, 2003.
[16] J. Reimann, M. Behnke, Experimental investigation of basic properties of monosized and binary Beryllium pebble beds, FZKA 6337 (1999).

[17] J. Reimann, H. Harsch, Thermal creep of Beryllium pebble beds, in: Proceeding 23rd SOFT, Venice, 2004.
[18] J. Reimann, S. Mueller, First experiments on the thermomechanical behaviour of Li_4SiO_4 pebble beds, in: Proceeding 20th SOFT, 1998.
[19] J. Reimann, G. Worner, Thermal creep of Li_4SiO_4 pebble beds, Fusion Eng. Des. 58–59 (2001) 647–651.
[20] ABAQUS, Theory Manual, Version 6.5, 2004.
[21] L. Buhler, J. Reimann, Thermal creep of granular breeder materials in fusion blankets, J. Nucl. Mater. 307 (2002) 807–810.
[22] J. Reimann, G. Piazza, H. Harsch, Thermal conductivity of compressed beryllium pebble beds, Fusion Eng. Des. 81 (2006) 449–454.
[23] J. Reimann, S. Hermsmeyer, Thermal conductivity of compressed ceramic breeder pebble beds, Fusion Eng. Des. 61–62 (2002) 345–351.
[24] J. Reimann, E. Arbogast, M. Behnke, S. Muller, K. Thomauske, Thermomechanical behaviour of ceramic breeder and beryllium pebble beds, Fusion Eng. Des. 49 (2000) 643–649.
[25] S. Hermsmeyer, J. Reimann, Particle flow of ceramic breeder pebble beds in bi-axial compression experiments, Fusion Eng. Des. 61–62 (2002) 367–373.
[26] L. Laloui, C. Cekerevac, Thermo-plasticity of clays: an isotropic yield mechanism, Comput. Geotech. 30 (2003) 649–660.
[27] L. Buhler, A simple model for the elasticity of granular materials in fusion breeding blankets, FZKA 6093 (1998).
[28] J. Duran, Sands, Powders and Grains, Springer, 1999.